Spatial and temporal variability of mode-1 and mode-2 internal solitary waves from MODIS/TERRA sun glint off the Amazon shelf.

Carina Regina de Macedo[1,2], Ariane Koch-Larrouy[2], José Carlos Bastos da Silva[3,4], Jorge Manuel Magalhães[3,5], Carlos Alessandre Domingos Lentini[6,7,8], Trung Kien Tran[1], Marcelo Caetano Barreto Rosa[7], and Vincent Vantrepotte[1]

[1]Univ. Lille, CNRS, Univ. Littoral Côte d'Opale, IRD, UMR 8187 - LOG - Laboratoire d'Océanologie et de Géosciences, F-59000 Lille, France
[2]LEGOS, Université de Toulouse, CNES, CNRS, IRD, UPS, Toulouse, France
[3]Department of Geosciences, Environment and Spatial Planning, Faculdade de Ciências da Universidade do Porto, Rua do Campo Alegre 687, 4169-007, Porto, Portugal
[4]Instituto de Ciências da Terra, Polo Porto, Universidade do Porto, Rua do Campo Alegre 687, 4169-007, Porto, Portugal
[5]CIIMAR, Universidade do Porto, Rua dos Bragas 289, 4050-123, Porto, Portugal
[6]Department of Earth and Environment Physics, Physics Institute, Ondina Campus, Federal University of Bahia—UFBA, Salvador, Bahia, Brazil
[7]Department of Oceanography, Geosciences Institute, Campus Ondina, Federal University of Bahia —UFBA, Salvador, Bahia, Brazil
[8]Interdisciplinary Center for Energy and Environment (CIEnAm), Federal University of Bahia UFBA, Salvador, Bahia, Brazil

Correspondence: Carina Regina de Macedo (carina.macedo@fc.up.pt)

Abstract. The Amazon shelf is a key region for intense internal tides (ITs) and nonlinear internal solitary waves (ISWs) generation associated with them. The region shows well-marked seasonal variability (boreal Summer/fall ASOND vs spring MAMJJ) of the circulation and stratification, which can both induce changes in the ISW physical characteristics. The description of the seasonal and neap-spring tidal variability of the ISWs off the Amazon shelf is performed for the first time using a meaningful data set composed of more than a hundred MODIS/TERRA imagery from 2005 to 2021, where more than 500 ISW signatures were identified in the sun glint region. Previous studies have documented the existence of mode-1 ISW, but the region appears as a newly described hotspot for mode-2 ISWs. ISWs packets separated by typical mode-1 (95 - 170 km; 2.1 - 3.8 $\mathrm{m.s^{-1}}$) and mode-2 (46 - 85 km; 1.0 - 1.9 $\mathrm{m.s^{-1}}$) ITs wavelengths have been identified and mapped coming from different IT generation sites. The mode-1 intra-packet (waves of the same packet) distance has a modal value of 10 km. Regions of higher occurrence of ISWs might correspond to the reflection beams at the surface. The mean mode-1 and mode-2 propagation velocities/wavelengths do not show significant differences according to their IT generation sites. A larger proportion of mode-2 waves is likely linked to shallower pycnocline with higher maximum values. The wave activity is higher during spring tides than neap tides. Mode-1 ISWs exhibit mean wave propagation velocities/wavelengths 14.3% higher during ASOND in the region under the influence of the North Equatorial Counter Current (NECC). In contrast, no seasonal variation of mode-2 propagation velocities/wavelengths was found. The reinforcement of the NECC appears to play a role in deviating the waves towards the northeast, increasing their phase velocities and their eastern traveling direction component which gives them an extra offshore acceleration. The impact of the circulation on the propagation velocities/wavelength is even more evident for mode-2 waves.

During ASOND, when the circulation has higher small-scale variability the ISWs propagate in a wider pathway and have a higher diversity of propagation velocities. Calculations of the IT velocities using the Taylor-Goldstein equation supported our results of the presence of ISWs associated with mode-2 IT and additionally into the ISW/IT seasonal variability.

Copyright statement. TEXT

1 Introduction

Nonlinear internal solitary waves (ISWs) are generated in the ocean by various processes, including the interaction of the flow with underwater sills/banks, and the evolution/disintegration of internal tides (ITs) (Jackson et al., 2012; Alford et al., 2015). Their turbulent mixing and strong horizontal and vertical currents have an impact on oceanic physical and biological processes (e.g., redistribution of heat, and momentum across oceanic basins, and nutrients supply for photosynthesis) (Sandstrom and Elliott, 1984; Huthnance, 1995; Munk and Wunsch, 1998; Muacho et al., 2013) while ISW can also represent a source of hazards for economic activities (e.g., aquaculture and offshore drilling operations) (Osborne et al., 1978; Hyder et al., 2005).

The Amazon shelf has been reported in the literature as being an important hotspot for intense internal tides (IT) and internal solitary waves (ISWs) generation (Brandt et al., 2002; Magalhães et al., 2016; Lentini et al., 2016; Bai et al., 2021; Tchilibou et al., 2022). Different works have already documented the presence of ISWs in the Amazon Shelf with studies illustrating their propagation both offshore (Brandt et al., 2002; Magalhães et al., 2016) and along the continental shelf (Lentini et al., 2016; Bai et al., 2021). The former is associated with IT hotspots generated over the steep slopes of the Amazon shelf break and disintegrate into short-scale waves several hundred kilometers from the shelf break (Magalhães et al., 2016). The shorter-scale ISWs are trapped in the IT troughs, both propagating together (Jackson et al., 2012). Magalhães et al. (2016) identified two regions (called A and B) as being the most energetic generation sites (see their Fig. 1). In Tchilibou et al. (2022), more than 6 sites of internal tide generation were identified along with the Amazon shelf break, A and B remaining the strongest.

Intra-seasonal to seasonal variability of the circulation and stratification and neap-spring tidal forcing are linked to changes in the IT and ISW propagation direction, intensity, wavelength, and, consequently, their velocities (Vlasenko et al., 2012; Magalhães et al., 2016; Liu and D'Sa, 2019; Tchilibou et al., 2022). The Amazon shelf is characterized by two seasons with well-marked differences in water stratification, surface currents, and mesoscale circulation. In boreal spring (from March to July, hereafter MAMJJ), the currents and mesoscale activity are weaker and the pycnocline is shallower, slightly stronger, and horizontally more homogeneous; during the boreal summer/fall (from August to December, hereafter ASOND), the currents and mesoscale activity are intensified and the pycnocline is deeper, slightly weaker and has a stronger horizontal gradient along with the North Brazil Current retroflection/North Equatorial Countercurrent (NBCR/NECC) path (Richardson and Walsh, 1986; Richardson et al., 1994; Silva et al., 2005; Aguedjou et al., 2019; Tchilibou et al., 2022). Seasonal variability of the ISWs in the region was linked to the seasonality of the NECC, which was pointed to as the mechanism responsible for refracting the waves toward the northeast and enhancing their velocities during the ASOND time period (Magalhães et al., 2016). The

seasonality of the pycnocline depth and strength was linked in the Amazon shelf to changes in the IT baroclinic mode and wavelength (Barbot et al., 2021; Tchilibou et al., 2022). Finally, the currents may interact with the IT field creating some refraction, branching, or even dissipation of the tidal baroclinic flux (Dunphy et al., 2017; Tchilibou et al., 2022). During ASOND, Tchilibou et al. (2022), in a realistic regional modeling configuration showed that the eddy kinetic energy is higher, and the mesoscale currents create a more energetic noncoherent baroclinic flux. This study further illustrated that the latter flux has numerous branching and deviations, and the internal tides field seems more diffuse. The impact of the water stratification and the seasonal variability was also discussed for mode 2 ITs off the Amazon shelf by Barbot et al. (2021); Tchilibou et al. (2022). Analyzing the vertical modal structure for mode-2 IT, a deeper pycnocline seems to shift the extrema of the modes toward intermediate water layers (i.e., the first extremum is deeper and the second one is shallower), decreasing the IT elevation amplitude and increasing its horizontal surface wavelength (with a lower impact on mode-2 than on mode-1) (Barbot et al., 2021). During MAMJJ, the shallower and slightly strong pycnocline seems to enhance the generation of higher baroclinic modes ITs, enhancing the local dissipation (Tchilibou et al., 2022).

In the study area, Magalhães et al. (2016) found ISWs with an average inter-packet distance with typical wavelengths of long (semi-diurnal) ITs of the fundamental mode (i.e., mode-1 ITs). However, the presence of small-scale ISWs with average inter-packet distance with a typical wavelength of mode-2 ITs was briefly reported in the region by da Silva et al. (2016). The authors denominated these smaller-scale features as wave tails. Signatures of small-scale ISWs trailing larger ISWs have been documented in the South China Sea, Mascarene Ridge of the Indian Ocean, and Andaman Sea (Guo et al., 2012; ?; da Silva et al., 2015; Magalhães and da Silva, 2018). In the South China Sea, simulations showed two different processes leading to short internal waves riding on mode-2 ISW and following a strong mode-1 ISW. The first one is related to the disintegration of a baroclinic bore, which is generated by the interaction between topography and tidal current. The second process calls for nonlinear interaction between mode-1 and mode-2 ISWs, which takes place when a faster mode-1 wave overtakes a mode-2 ISW generated one tidal cycle earlier (Guo et al., 2012). In Mascarene Ridge and the Andaman Sea, the impact of the IW beam with the pycnocline is pointed to as the mechanism responsible for the generation of mode-2 ISWs subsequently developing shorter-scale waves (wave tails with mode-1 structure) on its background (da Silva et al., 2015; Magalhães and da Silva, 2018). Potential mechanisms for the generation of mode-2 waves have been illustrated and they include the instability of shoaling mode-1 waves (Helfrich and Melville, 1986) and their interaction with localized sills (Lamb and Warn-Varnas, 2015), propagation of mode-1 waves into horizontally varying stratification regime (Liang et al., 2018) and shoaling mode-2 semi-diurnal internal tide (Liang and Li, 2019). Although the mode-2 waves are not as fast and energetic as the larger depression/elevation mode-1 waves, they potentially play a significant role in mixing and enhancing the fluxes of nutrients and heat in the water column because of their location in the middle of the pycnocline (Moum et al., 2008). The mode-2 waves receive less attention in the literature compared to mode-1 although some works are documenting mode-2 waves propagating with mode-1 tail in Knight Inlet, British Columbia (Farmer and Smith, 1980) and or illustrating their occurrence following mode-1 waves in the South China Sea (Yang et al., 2009; Liu et al., 2013).

Remote sensing (RS) is a key observation tool for providing new insights into the ISW generation, propagation, and dissipation mechanisms. Research efforts concerning ISWs are often based on synthetic aperture radar, SAR, and on optical images

acquired under sun glint conditions (i.e., areas where the sunlight specular or near-specular reflects directly to the sensor viewing angle) (Jackson and Alpers, 2010; da Silva et al., 2011; Liu et al., 2014; Magalhães et al., 2016). Signatures of oceanic features on sun glint imagery are produced by variations of short-scale sea surface roughness which cause changes in the image glitter brightness (Jackson and Alpers, 2010; Kudryavtsev et al., 2012). Since ISWs produce leading bands of rough followed by smooth sea surface roughness associated, respectively, with convergent and divergent surface currents, this oceanic feature can be observed in sun glint imagery (Alpers, 1985; Jackson and Alpers, 2010).

Here, we study the ISWs off the Amazon shelf using for the first time a comprehensive data set composed of more than a hundred images acquired by the Moderate Resolution Imaging Spectroradiometer (MODIS) onboard the TERRA satellite (Jan-2005 to Dec-2021). ISWs with inter-packet distance with typical wavelengths of mode-1 ITs and large-scale mode-2-like ISWs (wave tails with inter-packet distance with typical wavelengths of mode-2 ITs, i.e., waves which have a wavelength of order of kilometers being different from the classic mode-2 ISWs with the wavelength of the order of centimeters) have been mapped and their propagation velocities and directions are analyzed, considering their seasonal and neap-spring tidal variability. Calculations of the IT phase velocities using the Taylor-Goldstein equation (TGE) supported our results of the presence of shorter-scale ISWs tails separated by mode-2 IT wavelengths in the study area and additionally into the ISW/IT seasonal variability. For the first time, the Amazon shelf is described as an important hotspot for shorter-scale ISWs coupled with mode-2 ITs.

2 Data and Methods

2.1 Remote sensing and reanalysis data

The RS data set is composed of 140 images (acquired from 01 January 2005 to 31 December 2021) of Level 1B data from the MODIS sensor onboard the TERRA satellite. The images were acquired off the Amazon shelf where the presence of ISW signatures was identified in the sun glint region using Band 6 centered at 1640 nm with a spatial resolution of 500 meters. Level 1B MODIS/TERRA images were collected from NASA's Earth Science Data System, ESDS (https://earthdata.nasa.gov/). The cloud coverage (especially during the months of MAMJJ) and the position of the sun glint area, which changes its position over the year, are limiting factors for our samples.

The Global Ocean Ensemble Physics Reanalysis (EPR) data provides a 3D-gridded description of the global oceanic physical state at 0.25-degree resolution, starting from January 1993 until December 2019. The data is produced by Mercator Ocean International as part of the Copernicus Programme (https://marine.copernicus.eu/), using a multi-numerical ocean model (GLORYS2V4 from Mercator Ocean, France, ORAS5 from ECMWF, GloSea5 from Met Office, United Kingdom, and C-GLORSv7 from CMCC, Italy) ensemble approach and data assimilation of satellite and *in situ* observations. The daily mean average of temperature, salinity, and currents variables was acquired from 2005 to 2019 for 75 vertical levels.

2.2 Remote sensing processing

115   The ISW signatures were visually identified and manually extracted for each MODIS/TERRA scene of our data set. Signatures of non-linear ISWs can be visualized as leading bands of increased sea surface roughness followed by bands of decreased roughness (Alpers, 1985; Jackson and Alpers, 2010). The leading wave of each ISW packet was mapped for each image of our data set and the distance between two consecutive leading wave signatures (inter-packet distance, hereafter called wavelength since it is associated with typical IT wavelengths) was calculated considering the vector which connects the middle point of

120   each consecutive ISW signatures, perpendicular to the ISW crests. An image showing a typical view of this study region in which it can be seen that ISW signatures are often found with typical mode-1 and mode-2 IT wavelengths (hereafter called mode-1 and mode-2 internal waves) can be seen in Figure 1. The average wave propagation velocity was calculated considering the period of the semi-diurnal IT of 12.42 hours. The ISW propagation direction,, was automatically retrieved from the RS data considering the angle between the North and the direction of the vector which connects the middle point of two consecutive

125   packets (in a clockwise direction), i.e., $pd = 0°$ means ISWs propagating from the South to the North and $pd = 90°$ means propagating from West to East.
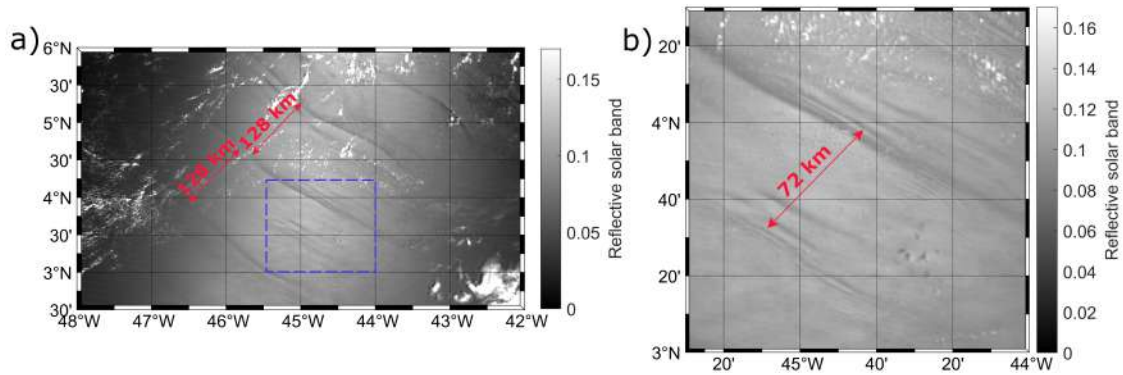
Figure 1. Level 1B MODIS/TERRA image, band 6, acquired on 10th October 2014 shows: (a) a typical view of this study region in which it can be seen that ISW signatures are often found with typical mode-1 IT wavelengths. The blue rectangle represents the area where (b) signatures associated with mode-2 ITs are found.

2.3 Theoretical calculation of IT velocities

The wave velocities of all modes are calculated using the numerical method proposed by (Lian et al., 2020) to solve the viscous TGE (see Appendix A). The approach is used to explain the existence of mode-2 IT waves off the Amazon shelf,

130   including the understanding of the wave's seasonal and near-spring tide variability in terms of shear and water stratification. The local values of stratification and shear were taken from daily and monthly EPR data for each location where ISWs were identified considering the entire period of time (from 2005 to 2019). The current velocities were decomposed in the ISW traveling direction. Here, positive velocity means current flowing in the same direction as the ISWs/IT; while a negative one
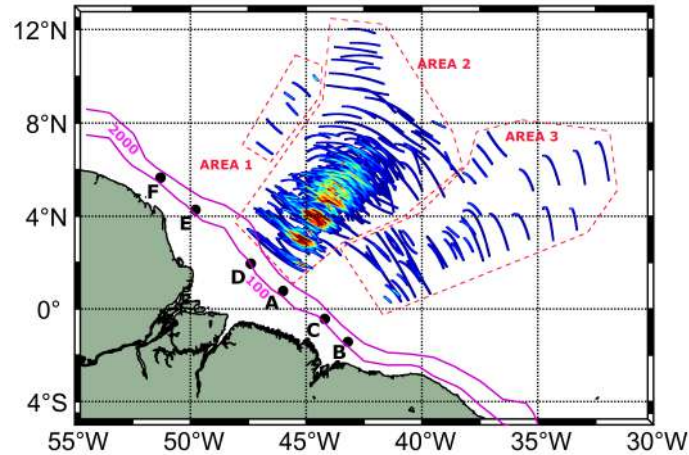
Figure 2. Spatial density map of occurrences of ISW signatures visible in MODIS/TERRA images. The points labeled from A to F are IT generation points, which are ordered according to their energy flux amplitudes following Tchilibou et al. (2022).

means current flowing in the opposite direction. The separation between the different wave modes is based on the probability

135 distribution of the velocities predicted by the viscous TGE for mode-1 and mode-2, considering the monthly EPR data.

2.4 Statistical analysis

The normality of the distribution associated with each considered parameter (ISW wavelength/velocity) was evaluated using the Shapiro-Wilk test, SWT. The comparison of the mean of the different groups of data considered here was then performed using a parametric test (Student t-test) when the distribution of the sample was following a normal distribution; while the non-

140 parametric test (Mann-Whitney-Wilcoxon Test, MWWT) was applied when this condition was not valid or for comparison of unbalanced size groups (number of samples in one group more than 3 times the number of samples of the other one). The non-parametric Kruskal-Wallis H test (KWT) was performed to determine if there are statistical differences among more than two independent groups. The non-parametric kernel density (KD) estimation was used for probability density estimation when a parametric distribution could not properly describe our variable.

145 **3 Results**

All ISW occurrences identified off the Amazon shelf found by direct examination of images are displayed in Figure 2. ISWs emanate from several IT generation sites along with the shelf break near the 500 m isobath as previously described by (Magalhães et al., 2016; Tchilibou et al., 2022). By analysis of the M2 baroclinic flux in the region (Tchilibou et al., 2022), we divided the waves into regions (Areas 1, 2, and 3) according to their likely associated IT generation sites. Area 1 may contain

150 waves from generation sites E and/or F and area 2 may contain waves from A and D sites. In area 3, ISWs likely come from B and/or C sites. A higher number of occurrences of waves is found in area 2, revealing coherent sub-patches (more than

35 occurrences) separated from each other by mode-1 typical wavelength (see Table 1), being the sub-patch further northeast structured as a tail with finer scales. The sub-patches are organized following a similar pattern as the one of the M2 internal tides dissipation described by Tchilibou et al. (2022). This suggests that when reflecting the surface or subsurface the internal
155   tides get unstable and generate strong ISW (Gerkema, 2001). The distance between IT generation site A (isobath of 100 m) and the first ISW sub-patch of higher occurrence in area 2 is around 150 km.

The first analysis was done considering the ISWs with intra-packet distances associated with mode-1 IT, Figure 3-(a) gives further insight into the horizontal structure of the northeastward-propagating waves, revealing a largely unimodal distribution of crest lengths that are strongly skewed toward the shorter end. These ISW packets are regularly observed to reach crest
160   lengths ranging up to 372 km, although most of the observations are characterized by crest lengths between 70 and 90 km. Unlike sun glint-derived wave identification, SAR-derived ISWs are generally unaffected by cloud cover. This could explain the skewed distribution here observed toward lower values due to the intense cloud coverage associated with the Inter Tropical Convergence Zone near the Amazon region. The intra-packet distance distribution, which is the distance between waves of the same packet, shows a unimodal distribution shifted to the smallest distances with most of the observations ranging between 7
165   and 18 km, with a modal value of $\sim$ 10 km (Figure 3-(b)). The average intra-packet distance for the entire period is 12 km with a standard deviation of 6 km.
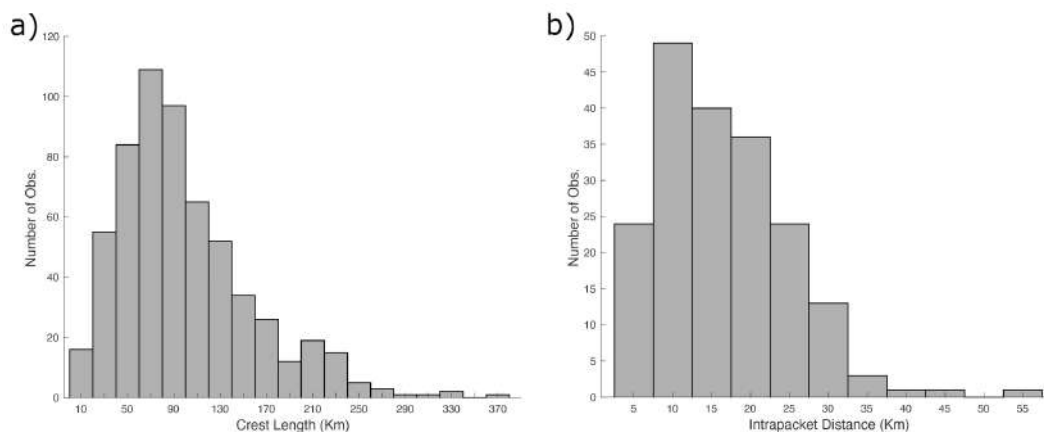
Figure 3. (a) ISW crest lengths. The average length is 99 km, with a standard deviation of 58 km. (b) ISW intra-packet distance distribution.

Table 1. Distance between the sub-patches of higher occurrence of ISWs in area 2. The first sub-patch correspond to the one further Southwest.

Higher occurrence sub-patches	Distance (km)
1 - 2	110
2 - 3	123
3 - 4	115

3.1 ISWs temporal distribution of first and second baroclinic modes

The monthly and yearly number of clear images and the number of signatures per clear image (i.e., the number of identified ISW signatures according to their modes divided by the total number of images containing at least one clear signature) are presented, respectively, in Figure 4-(a) and (b). The number of clear RS images is not equally distributed among the months, with most of the images (84%) being identified during the dry season (less cloudy coverage) from August to October. Because of the lack of acquisitions for some months, no evident seasonal variability is found. The mode-1 waves show a more homogeneous distribution according to the years; while the number of mode-2 waves has a more evident variation. The total number of detected mode-1 waves is about 3 times the number of mode-2.
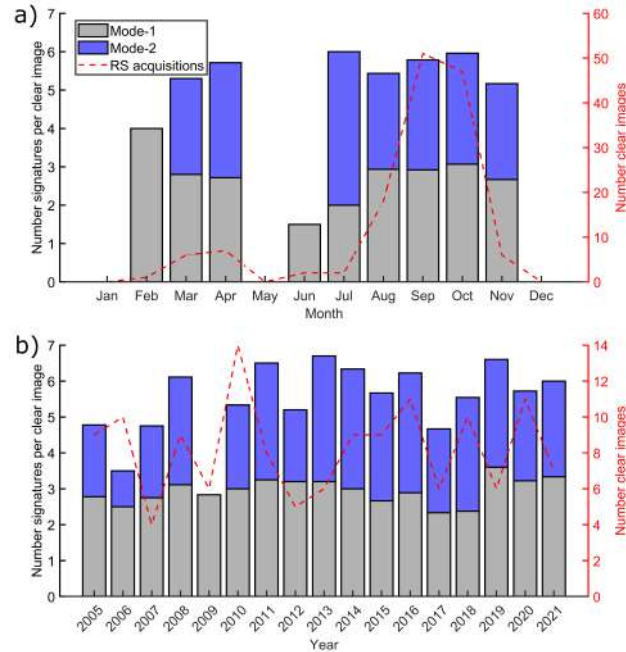
Figure 4. The monthly (a) and yearly (b) distributions of the number of RS images in which at least one ISW signature was identified (clear image), dashed red line, and the corresponding number of normalized mode-1 (gray bars) and mode-2 (blue bars) ISW signatures.

In area 2 (waves coming from IT generation sites A and D), the wave's propagation velocity/wavelength has a bi-model normal distribution (SWT, $\rho > 0.5$, see Figure 5-(a)), being each group likely associated with waves of different baroclinic modes (the group with higher mean velocity/wavelength calling for mode-1 waves, see Table 2). The mean mode-1 and mode-2 wavelength (velocity) deduced from the RS data are, respectively, 131.90 ± 16 km (2.94 ± 0.40 m.s^{-1}) and 70.40 ± 7.50 km (1.57 ± 0.20 m.s^{-1}). In the area, Magalhães et al. (2016) observed ISWs of fundamental mode propagating with similar mean velocities (i.e., 3.1 m.s^{-1}). Velocity/wavelength distribution calculated using TGE (Figure 5-(b)) shows for mode-1 and mode-2 waves a similar pattern to the RS measurements, supporting our decision to separate the ISWs according to the different baroclinic modes. The simulated mode-1 mean propagation velocity is underestimated by $\sim 20\%$. da Silva et al. (2011) found

Table 2. Values of IT wavelength and average propagation velocity calculated from RS data and predicted by solving the viscous TGE using monthly reanalysis data in areas 2 and 3 according to the different baroclinic modes of the waves.

Area	Baroclinic mode	Number of signatures	Data Source	Wavelength (km)		Propagation Velocity (m.s^{-1})	
				Mean ($\pm$ std)	Min–max	Mean ($\pm$ std)	Min–max
2	1	353	RS	131.90 ($\pm$ 16)	96.30–170.00	2.94 ($\pm$ 0.40)	2.20–4.00
			TGE	109.69 ($\pm$ 8.98)	76.36–146.18	2.45 ($\pm$ 0.20)	1.71–3.27
	2	103	RS	70.40 ($\pm$ 7.50)	46.40–84.20	1.57 ($\pm$ 0.11)	1.00–1.90
			TGE	70.41 ($\pm$ 4.98)	46.44–88.80	1.57 ($\pm$ 0.11)	1.04–1.99
3	1	19	RS	128.20 ($\pm$ 9.70)	109.80–141.95	2.87 ($\pm$ 0.20)	2.46–3.17
			TGE	104.61 ($\pm$ 4.82)	89.13–125.54	2.34 ($\pm$ 0.11)	1.99–2.81
	2	26	RS	69.40 ($\pm$ 11.60)	52.13–93.71	1.55 ($\pm$ 0.30)	1.17–2.10
			TGE	66.85 ($\pm$ 4.71)	50.54–82.32	1.50 ($\pm$ 0.11)	1.13–1.84

an underestimation of the phase speed calculated by the TGE of $\sim$ 12% in the Mascarene Plateau considering the ocean depth between 3 - 3.8 km. According to Alford et al. (2010), in the South China Sea nonlinear waves of M2 frequency travel at a phase speed 1.5 times the linear wave phase speed. The nonlinear phase speed is positively proportional to the surface wave elevation, which explains the higher underestimation of the mode-1 waves (Jeans, 1995; Barbot et al., 2021; Tchilibou et al., 2022).

In area 3 (waves coming from IT generation sites B and/or C), in contrast with area 2, the amount of mode-2 signatures is higher than mode-1 by 1.3 times (see Table 2). The depth of the pycnocline in the study area was defined as the depth corresponding to the maximal value of the Brunt–Väisälä frequency. A slightly shallower pycnocline with higher maximum values of the Brunt–Väisälä frequency is found in area 3 (see Figure 6-(a)), suggesting that stronger higher mode internal tide generation is expected (Barbot et al., 2021; Tchilibou et al., 2022) in good agreement with our findings. The wave propagation velocity/wavelength distribution has a bi-modal normal distribution similar to area 2 (Figure 5-(c)). The mean mode-1 and mode-2 wavelength (velocity) deduced from the RS data are, respectively, 128.20$\pm$9.70 km (2.87$\pm$0.20 m.s^{-1}) and 69.40$\pm$11.60 km (1.55$\pm$0.30 m.s^{-1}). For ISW of the fundamental mode, Magalhães et al. (2016) found waves with similar mean propagation velocity in area 3 (i.e., 2.7 m.s^{-1}). The TGE allows a relevant prediction of the propagation velocity/wavelength distribution of mode-1 and mode-2 waves, with mode-1 velocities being underestimated by 22% (Figure 5-(d)). The mode-1 and mode-2 mean propagation velocity/wavelength values do not vary significantly according to the different study areas ($\rho > 0.5$, MWWT).

Looking now at their horizontal distribution, mode by mode (Figure 7), the analysis of the mode-2 signatures clearly shows wave signatures emanating from the D site and joining area 2 (see a green rectangle in Figure 7-(b)). This example of joining rays of propagation may explain why this region is the strongest as it focuses rays from D as well. Considering the small
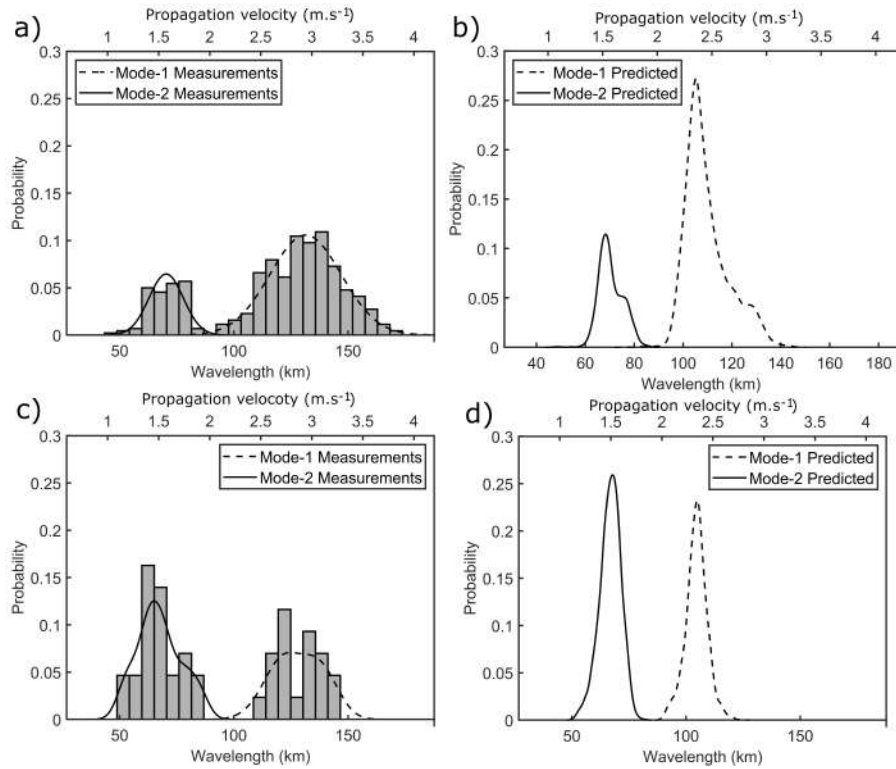
Figure 5. Histogram of mode-1 and mode-2 internal waves for (a) area 2 and (c) area 3 in gray color. The fitted normal distribution of the ISW propagation velocity/wavelength calculated from the RS data is shown in black. KD of the predicted velocities by solving the viscous Taylor-Goldstein equation using monthly reanalysis data for (b) area 2 and (d) area 3. Mode-1 and mode-2 waves are shown as dotted and continuous lines, respectively.
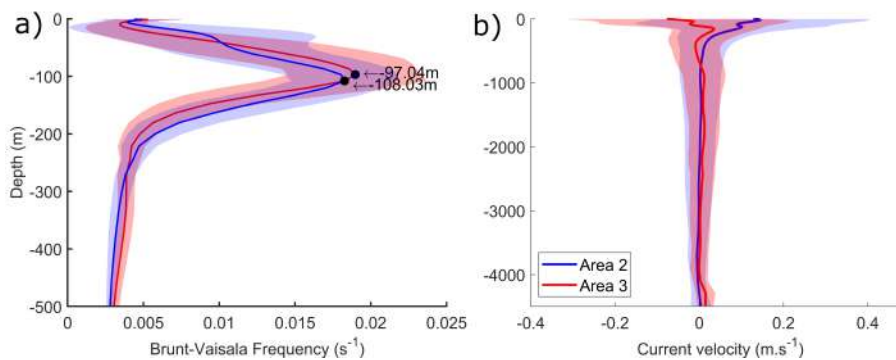
Figure 6. (a) Brunt-Väisäla frequency and (b) mean current velocity decomposed along the ISW traveling direction for areas 2 and 3 derived from ensemble physics reanalysis data. The bands represent the standard deviation over the period from 2005 to 2019.

number of signatures that come from area 1, the analysis presented in our paper does not consider those signatures. However, combining other satellite sensors might help retrieve a stronger signal from this site (Rosa et al., 2021).

205   The spatial distribution of the mode-1 and mode-2 waves according to their propagation velocities (respectively, Figure 8-(a) and (b)) allows the discrimination of two main branches of waves propagating in different directions in area 2, where the most eastern branch is associated with higher propagation speed. Globally a higher contrast is found for the branches of the mode-2 waves in terms of both velocities and spatial location when compared to mode-1. In area 2, an offshore acceleration is also further observed for the most eastern branch of both mode-1 and mode-2 waves (see Figure 8-(c) and (d), where a cross-shore

210   profile was done and the corresponding values of internal wave wavelengths along the profile were retrieved). The acceleration
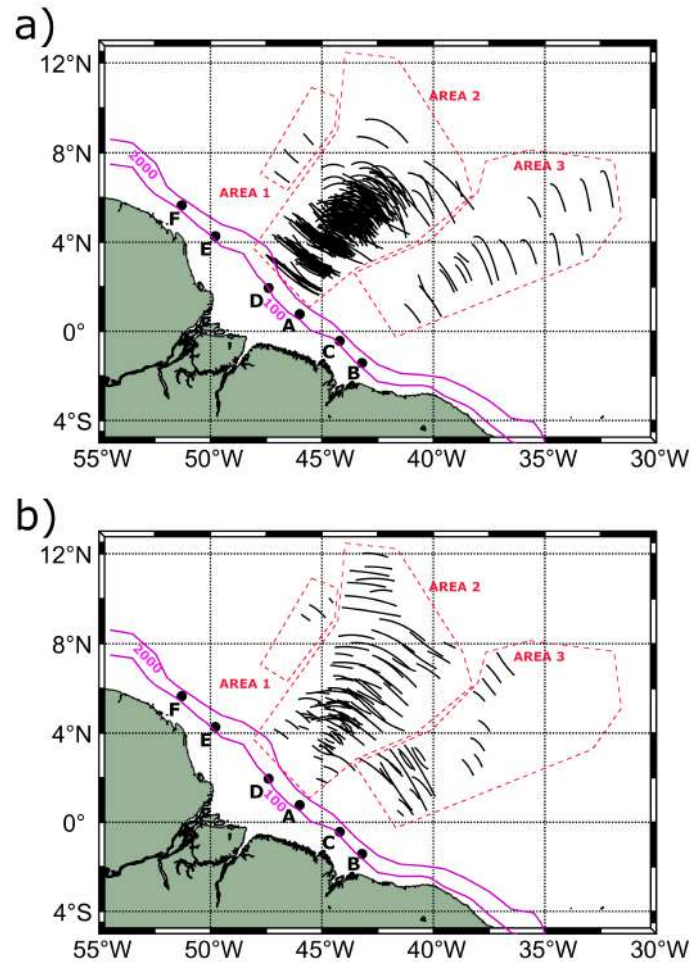
Figure 7. (a) mode-1 and (b) mode 2 ISW composite map derived from 140 MODIS/TERRA data acquired under sun glint conditions from 2005 to 2021. All identified signatures were considered and depicted on the map, with a total of 507 signatures among which 377 are associated with mode-1 and 130 correspond to mode-2 internal waves.

is slightly more pronounced for mode-2 waves with an offshore increment in the propagation velocities of $\sim 18\%$; while the increment for the mode-1 waves is $\sim 15\%$.

The characterization of the propagation direction of the ISWs (Figure 9) shows us that, in area 2, mode-2 waves propagate in a wider range of direction compared to mode-1 ones. The mean velocities/wavelengths tend to increase with the increase of the eastern traveling direction component (For both mode-1 and mode-2, there are significant differences between the ISW propagation direction paths, i.e., $\rho < 0.01$, KWT, Table 3). This increasing pattern is even more pronounced for the mode-2 waves than for mode-1 (respectively, an increase of 20% and 15%). This suggests that when deviated to the east the waves are accelerated by regional eastward currents.

In area 3, for both mode-1 and mode-2, waves for the different propagation paths do not differ statistically in terms of their velocity/wavelength ($\rho > 0.5$, respectively, MWWT and t-test). Area 3 is less influenced by the NECC than area 2. As a matter of fact, current velocities decomposed on the ISW traveling direction are less than half of the respective values found in area 2 with a higher negative component (i.e., the current flowing in the opposite direction to the waves traveling direction, Figure 6-

Table 3. Internal tide wavelength and average propagation velocity calculated from RS data in areas 2 and 3 according to the different baroclinic mode of the waves and their propagation directions.

Area	Order of baroclinic mode	Pd path (°)	Mean wavelength ($\pm$ std) (km)	Mean propagation velocity ($\pm$ std) ($m.s^{-1}$)
2	1	12	120.6 ($\pm$ 14)	2.7 ($\pm$ 0.4)
		36	132.4 ($\pm$ 15.2)	3.0 ($\pm$0.3)
		60	137.8 ($\pm$ 15.5)	3.1 ($\pm$ 0.3)
	2	12	68.6 ($\pm$ 9.0)	1.5 ($\pm$ 0.2)
		36	71.6 ($\pm$ 6.6)	1.6 ($\pm$ 0.1)
		60	73.9 ($\pm$ 6.7)	1.7 ($\pm$ 0.2)
3	1	348	64.7 ($\pm$ 2.8)	1.4 ($\pm$ 0.1)
		36	130.1 ($\pm$ 8.4)	2.9 ($\pm$ 0.2)
		60	132.2 ($\pm$ 11.5)	3.0 ($\pm$ 0.3)
		84	123.6 ($\pm$ 6.7)	2.8 ($\pm$ 0.1)
	2	12	93.7	2.1
		36	67.3 ($\pm$ 4.8)	1.51 ($\pm$ 0.1)
		60	65.1 ($\pm$ 10.5)	1.46 ($\pm$ 0.2)
		84	77.3 ($\pm$ 10.5)	1.7 ($\pm$ 0.2)

(b)). The stronger dynamic circulation during the boreal spring in area 2 (Richardson and Walsh, 1986; Richardson et al., 1994; Silva et al., 2005; Aguedjou et al., 2019) appears to significantly act on the wave velocities according to the different paths.
225 Compared with the mode-1 waves, the mode-2 ones have a stronger northern component and propagate in a wider pathway in both areas. In area 3, mode-1 and mode-2 waves have a more eastern traveling direction component.

3.1.1 Spring-neap tidal variability

The occurrence of ISWs according to the tidal conditions (i.e., near neap and spring tides) has been investigated for both areas 2 and 3. Near spring tide is defined as ± 7 days after spring tide peak. A more detailed description of wave propagation velocities
230 and directions variability according to the spring-neap cycle was performed in area 2 but not in area 3 because of the lack of measurements in that area.

Analysis of the RS data revealed that the ISW activity is more pronounced near spring tide conditions for both areas (71% of the ISWs signatures for area 2 and 61% for area 3). This result is in line with former studies where higher wave activity near
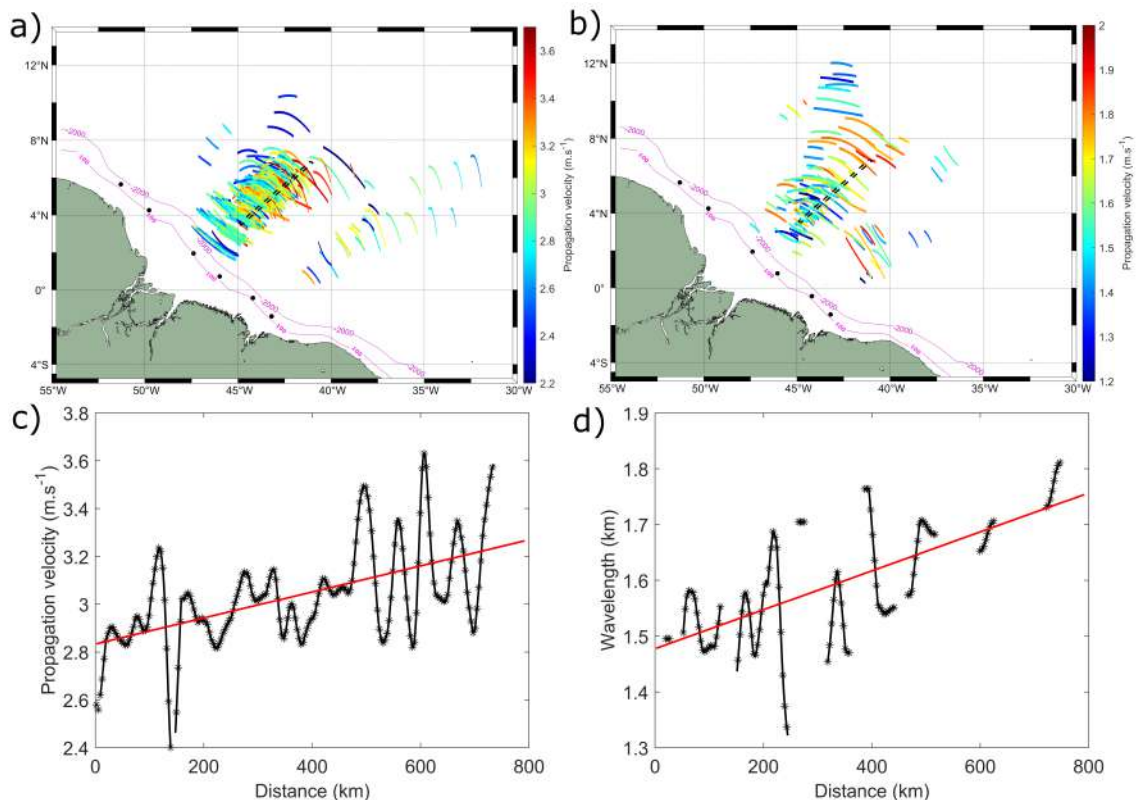
Figure 8. Propagation velocities of the (a) mode-1 (b) and mode-2 internal waves off the Amazon shelf. The black dashed rectangle represents the selected cross-shore profile. Cross-shore profile of the ISW propagation velocities for (c) mode-1 and (d) mode-2 waves derived from the RS data. The red line is the fitted linear regression model for the measurements.

spring tide has been reported (New and da Silva, 2002; da Silva et al., 2011; Liu and D'Sa, 2019). In both areas, there are more mode-2 waves during neap tides than spring tides (near neap and spring tide, in area 2, respectively 28% and 20%, and, in area 3, 61% and 48%).

For area 2, the mode-1 mean propagation velocity/wavelength varies according to the different tidal conditions ($p < 0.01$, t-test, Figure 10-(a)). Higher values are associated with the wave signatures found near neap tide (137.6±15.2 km and 3.1±0.3 m.s^{-1}); in contrast, near spring tide, the mean propagation velocity/wavelength of the waves decreases by about 6% (129.8±16.1 km and 2.9±0.4 m.s^{-1}). For the mode-2 waves, no significant differences are found according to the tide conditions ($p > 0.05$, t-test), see Figure 10-(b). The mean wavelength (propagation velocity) for near spring and neap tides are, respectively, 70.16±7.59 km (1.57±0.17 m.s^{-1}) and 70.67±7.55 km (1.58±0.17 m.s^{-1}). No significant differences are found in the propagation direction according to the spring-neap tides, for both mode-1 and mode-2 waves (figure not shown).

3.1.2 Seasonal variability

The seasonal variability of the ISW in terms of velocity, wavelength, and propagation direction has been further characterized considering the two well-marked seasons in the Amazon shelf, i.e. the boreal spring (MAMJJ) and the boreal summer/fall (ASOND) following Tchilibou et al. (2022). We only apply this analysis to the waves in area 2, because of the lack of measurements during MAMJJ in area 3. The mode-1 waves have 14.3% higher mean propagation velocity/wavelength during ASOND ($p < 0.01$, MWWT, see Figure 11-(a) and Table 4). The pycnocline during ASOND is slightly deeper when compared
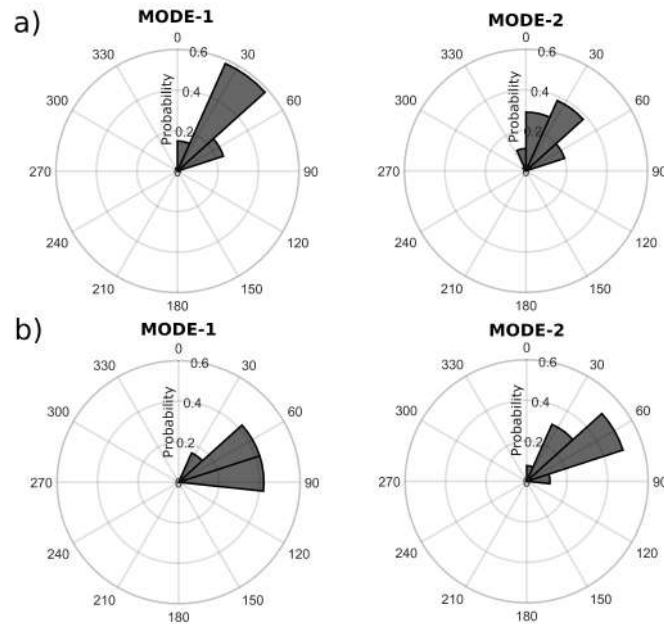
Figure 9. ISW propagation directions for (a) area 2 and (b) area 3. ISW propagation angles are clockwise from the North. A $pd = 0°$ denotes ISWs propagating from the South to the North and $pd = 90°$ denotes ISWs from the West to the East.
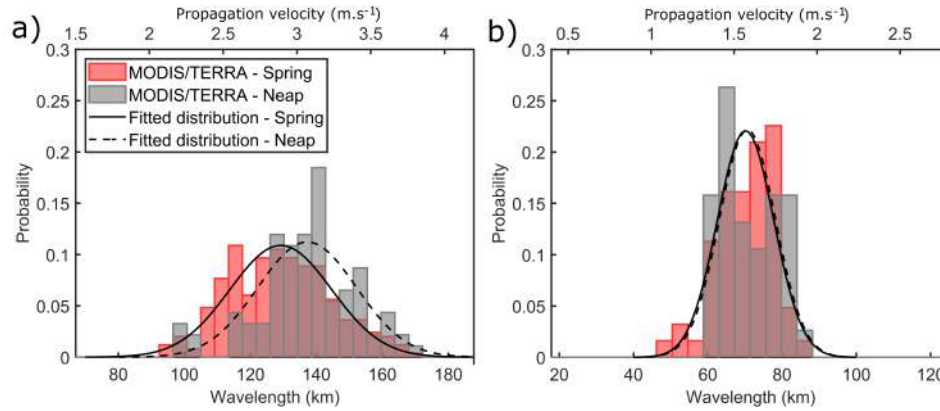
Figure 10. Fitted Gaussian distribution of the (a) mode-1 and (b) mode-2 internal wave propagation velocity/wavelength according to the neap (dotted line) and spring (continuous line) tides.

250 to MAMJJ (by 11 m, see Figure 12-(a)). Larger wavelengths (higher velocities) of mode-1 internal tides are expected during ASOND following previous studies (Liu and D'Sa, 2019; Barbot et al., 2021; Tchilibou et al., 2022). Furthermore, the mean current velocity decomposed on the ISW traveling direction has a stronger positive component during ASOND when compared to MAMJJ (Figure 12-(b)). Hence circulation and stratification probably act constructively to increase the wavelength during ASOND, in contrast to MAMJJ. Furthermore, during ASOND, the waves are characterized by a higher diversity in terms of

255 their wavelengths (higher standard deviation) when compared to MAMJJ, suggesting a higher variability of the local stratification and current shear patterns in the study area during the boreal summer/fall. Note that our samples are unbalanced according to the season, i.e., during ASOND we have about 8 times more samples than for MAMJJ.

The TGE is able to predict the differences in the mode-1 IT velocities/wavelengths between the two seasons ($p < 0.01$, MWWT) with a distribution pattern similar to the one estimated using the RS data (see Figure 11-(b)). However, the differences

260 between the two seasons are less evident considering the values predicted by the TGE (mean wavelength value increases by 9.5% during ASOND when compared to MAMJJ). Compared to the RS data, the mean waves' wavelength are underestimated by 11% and 14%, respectively, for MAMJJ and ASOND (Table 4). The mean velocity/wavelength values predicted using daily and monthly reanalysis data are very similar for both seasons. Differences in their standard deviation (standard deviation slightly higher for daily reanalysis data) indicate that using monthly data probably tends to smooth the variability related to

265 stratification and circulation.

The mode-2 propagation velocity/wavelength does not vary according to the different seasons ($p > 0.05$, MWWT), see Figure 11-(c) and Table 4. In contrast, the mean propagation velocities/wavelength calculated by the TGE is 4.6% higher during ASOND and, during this season, the distribution of the predicted velocities fits quite well with the RS data. The TGE seems to underestimate the wave propagation velocities by 6.5% during MAMJJ. It is important to point out that the mode-2

270 signatures identified from the RS observation are not well balanced between the seasons and the period of MAMJJ count with only 13 samples probably impairing our analysis.
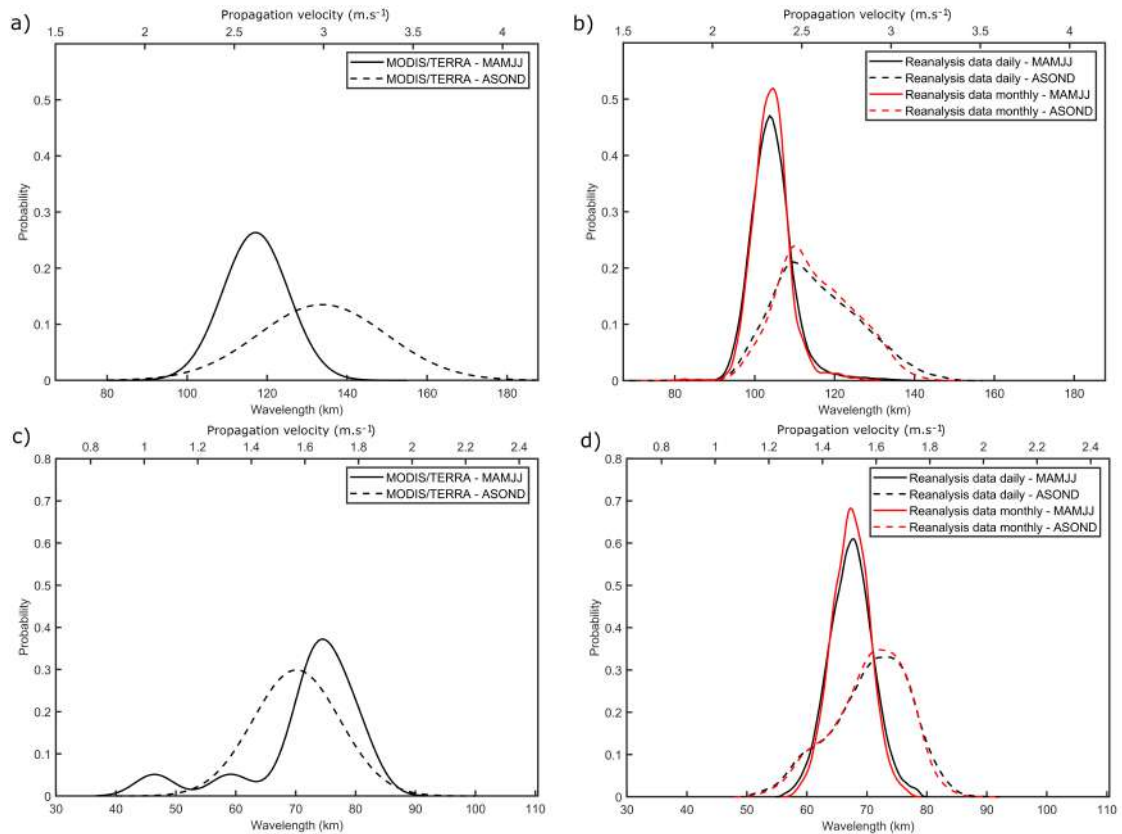
Figure 11. Fitted distribution of the ISW propagation velocity/wavelength calculated from the RS data for (a) mode-1 and (c) mode-2 waves for area A. Fitted distribution of the ISW propagation velocity/wavelength predicted by solving the viscous Taylor-Goldstein equation using daily and monthly reanalysis data, respectively, black and red lines for (b) mode-1 and (d) mode-2 waves. MAMJJ and ASOND are shown, respectively, as continuous and dashed lines.

During ASOND, the mode-1 and mode-2 waves propagate in a wider direction pathway (Figure 13), and an increase in the wave propagation velocities with increasing eastern traveling directions is found (no differences in the velocities of the waves are found during MAMJJ, $p > 0.05$, Mann-Whitney U nonparametric test). Higher differences during ASOND are found for
275 the mode-2 waves, which seem to be more sensitive to changes in the circulation patterns in the study area. In the months of ASOND, the circulation is characterized by the eastward reinforcement of the NECC, which likely plays a role in refracting the waves to the northeast (as pointed as well by Magalhães et al. (2016)) and in increasing their propagation velocities eastward. Furthermore, as a consequence of the more dynamic mesoscale circulation associated with ASOND, the ISWs seem to spread over the study area during this season (Figure 14), extending the wave penetration further north principally at the end of the
280 summer and early fall (August-October) when maximum values of eddy vorticity are found (Aguedjou et al., 2019). This behavior contrasts with the more straightforward path and lower penetration further north associated with the waves in the
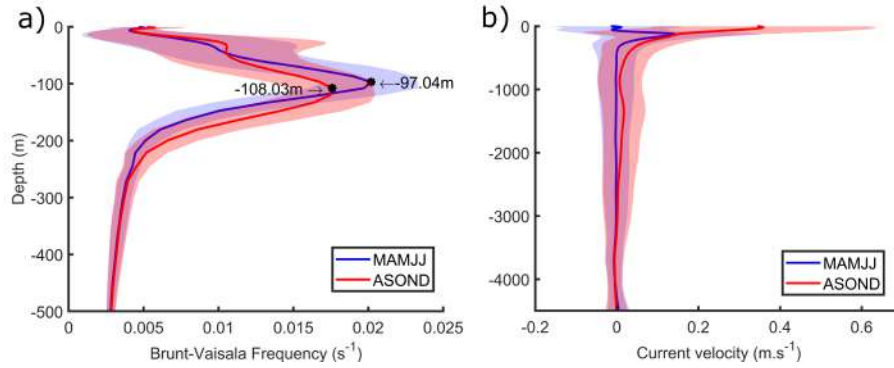
Figure 12. Fitted distribution of the ISW propagation velocity/wavelength calculated from the RS data for (a) mode-1 and (c) mode-2 waves for area 2. Fitted distribution of the ISW propagation velocity/wavelength predicted by solving the viscous Taylor-Goldstein equation using daily and monthly reanalysis data, respectively, black and red lines for (b) mode-1 and (d) mode-2 waves. MAMJJ and ASOND are shown, respectively, as continuous and dashed lines.

Table 4. Values of IT wavelength and average velocity calculated from RS data and predicted by solving the viscous TGE using daily and monthly reanalysis data in area 2 according to the seasons and the different baroclinic modes of the waves.

Season	Order of baroclinic mode	Data source	Wavelength (km)		Propagation velocity $(m.s^{-1})$	
			Mean ($\pm$ std)	Minimum - maximum	Mean ($\pm$ std)	Minimum - Maximum
MAMJJ	1	RS	117.1 ($\pm$ 8.2)	100.16 - 137.84	2.62 ($\pm$ 0.18)	2.24 - 3.08
		TGE - daily	104.35 ($\pm$ 5.52)	74.88 - 145.15	2.34 ($\pm$ 0.12)	1.68 - 3.25
		TGE - monthly	104.18 ($\pm$ 4.71)	80.96 - 128.84	2.33 ($\pm$ 0.11)	1.81 - 2.87
	2	RS	71.83 ($\pm$ 9.47)	46.43 - 81.89	1.61 ($\pm$ 0.21)	1.03 - 1.83
		TGE - daily	67.41 ($\pm$ 3.85)	45.72 - 88.43	1.51 ($\pm$ 0.09)	1.02 - 1.98
		TGE - monthly	67.37 ($\pm$ 3.30)	56.51 - 84.83	1.51 ($\pm$ 0.07)	1.27 - 1.90
ASOND	1	RS	133.8 ($\pm$ 16.1)	96.32 - 178.99	2.99 ($\pm$ 0.36)	2.15 - 4
		TGE - daily	115.62 ($\pm$ 10.95)	72.00 - 153.57	2.59 ($\pm$ 0.25)	1.61 - 3.44
		TGE - monthly	115.36 ($\pm$ 9.64)	77.67 - 145.95	2.58 ($\pm$ 0.22)	1.74 - 3.27
	2	RS	70.13 ($\pm$ 7.25)	53.09 - 84.24	1.57 ($\pm$ 0.16)	1.19 - 1.88
		TGE - daily	70.52 ($\pm$ 6.72)	36.31 - 90.24	1.58 ($\pm$ 0.15)	0.81 - 2.02
		TGE - monthly	70.48 ($\pm$ 6.24)	46.10 - 87.73	1.58 ($\pm$ 0.14)	1.03 - 1.97

months of MAMJJ. Most of the ISW signatures in area 2 above the latitude 8°N corresponds to mode-2 waves from early
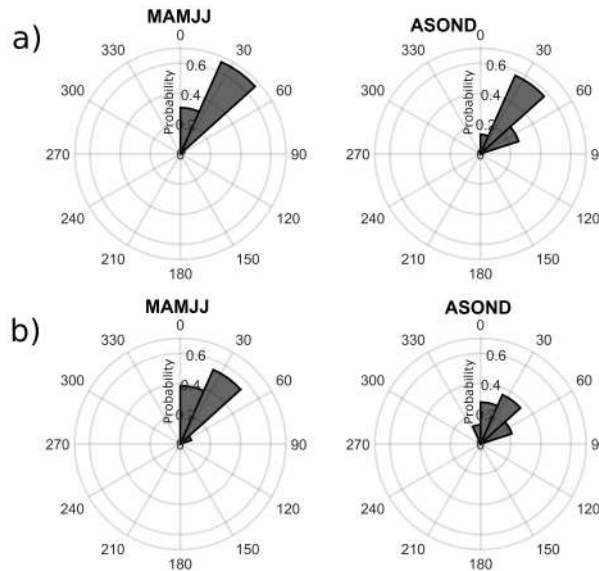
Figure 13. ISW propagation directions for (a) mode-1 and (b) mode-2 waves in area 2 according to the season. ISW propagation angles are clockwise from the North. A pd = 0° denotes ISWs propagating from the South to the North and pd = 90° denotes ISWs from the West to the East.

September 2014 and 2018. However, it is important to point out that this can result from sampling restrictions due to the combination of higher cloudy coverage and the location of the sun glint area during the months of MAMJJ.
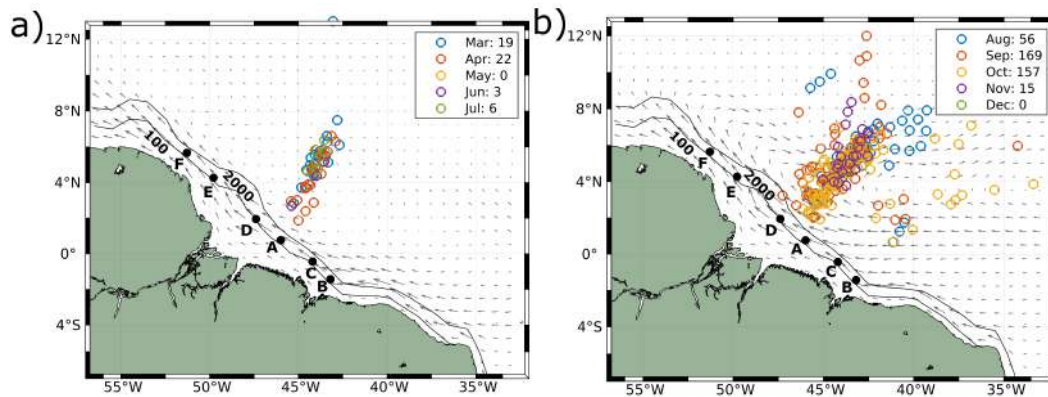
Figure 14. Location of the ISW signatures associated with mode-1 and mode-2 internal tides for (a) MAMJJ and (b) ASOND. The colors represent the months when the signatures were identified. The points represent the middle point of each wave signature and the arrows depict the mean surface current speed and direction for each season derived from the EPR data. The number of ISW signatures occurring per month can be found in the legend.

The time-space variability of the waves' phase velocity associated with changes in the background current and stratification is exploited as a proxy of the variability of the waves' propagation direction (refraction). Maps of the seasonal coefficient of variation of the mode-1 and mode-2 IT phase velocities calculated by the TGE using monthly average EPR data are shown in Figure 15. Changes in the phase velocity are more evident for mode-2 waves than mode-1 ones in both seasons, in good agreement with our results which show mode-2 waves as probably more sensitive to changes in the circulation patterns in the study area. In area 2 (waves coming from IT generation point A and D), the variability in the phase velocity is higher during ASOND than during MAMJJ. Furthermore, during ASOND the variability is aligned with the core of the NECC, in good agreement with our results. In area 3, a different pattern occurs since higher variability is found during the MAMJJ. However, further analysis in that area is compromised because of the lack of measurements.
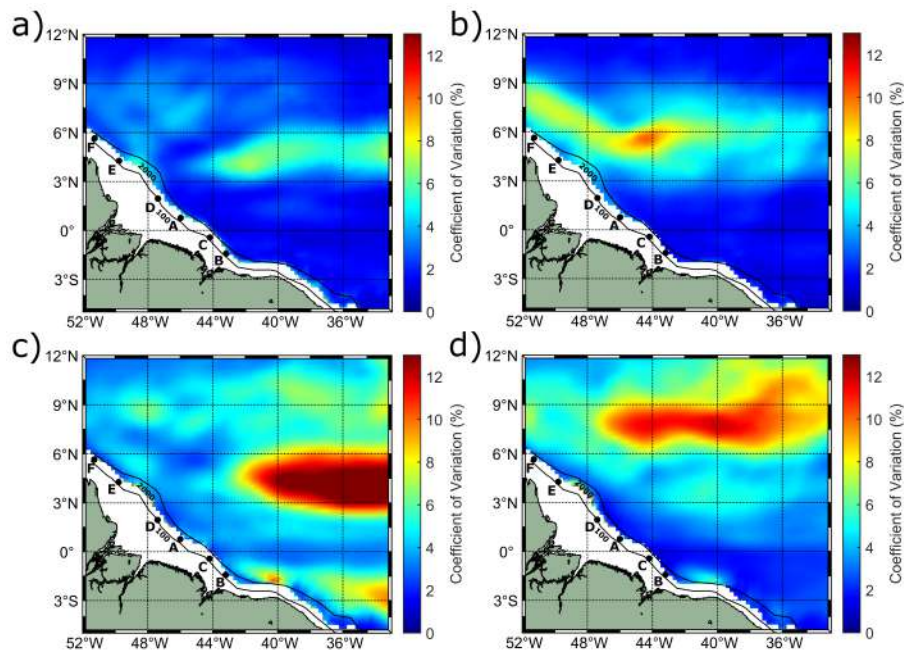
Figure 15. Maps of the seasonal coefficient of variation of the (a,b) mode-1 and (c,d) mode-2 IT phase velocities calculated by the TGE using monthly average EPR data for (a,c) MAMJJ and (b,d) ASOND.

4   Summary and discussion

This study focuses on the Amazon ISW occurrence and parameters, such as position, velocity, direction of propagation, wavelength, and variability at seasonal and spring-neap tidal cycles. The analysis is based on a data set of more than 100 MODIS-/TERRA images, where more than 500 ISW signatures were identified in the sun glint area.

Area 2 has been pointed out in our analysis as the one with stronger ISW activity containing more than 450 signatures, likely because it focuses rays emanating from both sites A and D. The region where the waves from A and D join the same

path corresponds to the third patch of occurrence from the shelf break, with higher occurrences (see Figure 2). Tchilibou et al. (2022) found IT generation sites A and B with quite similar M2 baroclinic flux horizontal divergence but site A being more efficient in converting the flux into ITs. In area 2, the distance between generation point A (isobath of 500 m) and the first patch of high occurrence is around 150 km. Regions of higher occurrence of ISWs are structured into sub-patches separated from each other by mode-1 typical wavelength (see Table 2) which might correspond to the reflection beams at the surface. Gerkema (2001) discussed the local wave activity in the thermocline in the Bay of Biscay due to the scattering of the internal-tide beam, which scatters strongly at a moderately developed thermocline. The patch further northeast is structured as a tail with finer scales, being noisier as the wave gets unstable to higher modes. The waves propagate about 350 km without dissipation and then suffer changes in their wavelength which could indicate some instability, a transfer to higher modes, or dissipation. Our finds are suitable with the results presented in Tchilibou et al. (2022).

Previous studies have documented the existence of mode-1 ISW (Magalhães et al., 2016), but in fact, the region appears as a newly described hotspot for large-scale mode-2-like waves with scale (wavelength) associated with mode-2 internal tides. The coexistence of mode-2 solitary-like waves and mode-1 ISW has been documented in the literature, for example, on the Mascarene Ridge (da Silva et al., 2015) and on the Andaman Sea (Magalhães and da Silva, 2018; Magalhaes et al., 2020). The ISW velocity/wavelength deduced from the RS data showed a bi-modal distribution with two well-separated peaks for both areas 2 and 3, allowing us to separate the ISW associated with two IT baroclinic modes: wavelength (velocity) ranging from 95-170 km (2.1-3.8 $m.s^{-1}$) for mode-1 and 46-85 km (1.0-1.9 $m.s^{-1}$) for mode-2. Barbot et al. (2021) found using results from ocean modeling horizontal surface wavelengths varying from 110-120 km and 70-80 km for mode-1 and mode-2 ITs in the study area which is in fair agreement with our results considering that nonlinear effects associated with the ISWs increase the phase speed of the waves and the variability of current and stratification that explain our more dispersive results compared to the model. Zhang and Li (2022) found a bi-modal distribution of the ISW phase speed in the region as well, calculating using a data-driven machine learning model ISW with a wide range of velocities from values lower than 1 $m.s^{-1}$ up to 4 $m.s^{-1}$. Although the underestimation of the mode-1 wavelengths/velocities by the TGE in the study area are of the order of 20-22%, the simulated wavelengths/velocities showed two well-separated distributions for mode-1 and mode-2 waves with a similar pattern to the one deduced from the RS data supporting our decision to split the waves according to their different baroclinic modes.

The range and values of mode-1 and mode-2 propagation velocities/wavelengths do not show significant differences according to areas 2 and 3. However, area 3 seems to have a higher proportion of mode-2/mode-1 waves (i.e., stronger higher mode internal tide generation) likely linked to its shallower pycnocline with higher maximum values when compared to area 2 (see Figure 6). However, we can not rule out the fact that ISWs emanating from IT generation site C may be influencing these results since according to Tchilibou et al. (2022) site C is the one most favorable to local dissipation (higher modes generation connected to a higher probability of instability, thus higher local dissipation). In both areas, neap-spring tidal variability is found, i.e., the wave activity is higher during near spring tides, which is coherent with the larger tidal currents during spring tides. This result is in line with former studies where higher wave activity near spring tide conditions has been also pointed out

(da Silva et al., 2011; Liu and D'Sa, 2019). In addition, the proportion of mode-2/mode-1 waves seems to increase from spring
335   to neap tide conditions.

Seasonal variability of the mode-1 waves was found in area 2, where a higher diversity (higher standard deviation) and higher values of wave propagation velocities/wavelengths were noticed during ASOND in contrast to MAMJJ (mean speed 14.3% higher). The joint effect of higher values of mean background current velocities along the ISW traveling direction and a deeper pycnocline but less stratified (smaller N2, see Figure 12) may explain the increase of the propagation velocities/wavelength of
340   the waves during the boreal summer/fall in agreement with Barbot et al. (2021); Tchilibou et al. (2022). Barbot et al. (2021) found that a deeper pycnocline due to large anticyclonic eddies of the NBC mostly from August to November increases the horizontal surface wavelengths of both mode-1 and mode-2 IT with a stronger impact on mode-1. No seasonal changes of mode-2 propagation velocities/wavelengths are found in contrast to the mode-1 ones. However, it is important to point out that the limited number of mode-2 wave samples in area A during MAMJJ likely impaired our analysis. Using the TGE, the
345   seasonal variability of predicted mode-1 and mode-2 waves was examined. Although the differences in the mode-1 propagation velocities/wavelength between ASOND and MAMJJ are underestimated by the theoretical method, TGE could reproduce the seasonal differences of the IT wavelength giving us confidence in our previous results and supporting our analysis principally considering our unbalanced data set according to the seasons. Furthermore, the TGE could reproduce the higher diversity of ISWs in terms of wavelength during the period of ASOND in agreement with our satellite measurements.
350   Finally, the comprehensive data set constructed during our analysis will support further studies to assess the impact of ISWs on the biological/biogeochemical dynamics in the study area with an emphasis on their impact on the phytoplankton biomass spatial-temporal variability.

Impact of NBC

The circulation can likely be pointed to as one important factor in the change of the velocities of the waves according to
355   the different propagation direction paths. The eastward reinforcement of the NECC during ASOND seems to play a role in refracting the waves northeast in area 2, increasing their velocities with increasing east traveling direction component and giving them an extra offshore acceleration. Magalhães et al. (2016) found an increase of 30% in the mode-1 ISWs velocities during ASOND based on the study of two showcases (one of them from May and the other one from October). The authors associated the seasonal differences in the propagation velocities/wavelengths with the variability of the NECC, which refracts
360   the wave and provides an additional (positive) component along the ISW traveling direction. In our study, the impact of the circulation in the propagation velocities/wavelength is more evident for mode-2 waves. According to Rainville and Pinkel (2006), the mesoscale ocean circulation changes the ISW propagation path, and group and phase velocities of all wave modes, however, the impact increases with the increasing of the mode numbers. Furthermore, the presence of waves with higher diversity in terms of their propagation velocities propagating in a wider pathway (see Figure 14) during ASOND seems to be
365   connected to the intensification of the currents and mesoscale activity in this season, which brings a higher variability in the shear/circulation conditions.

According to Tchilibou et al. (2022), during MAMJJ the mode-1 and mode-2 baroclinic fluxes from IT generation point A (contained in area 2) propagate further north than during ASOND. The stronger circulation and mesoscale activity during

the latter season are pointed as factors that largely block the energy flux at 6°N. The IW signatures mapped from RS data do not reproduce that behavior as it may be due to our sample restrictions during MAMJJ. During ASOND, the baroclinic flux is eastward deviated by the background circulation east of 45°W (Tchilibou et al., 2022). This behavior is reproduced by the IW signatures which seem to be laterally spread in the study area (refracted northeast) by the reinforcement of the NECC (see Figure 14). Furthermore, during ASOND the flux coming from the IT site D (contained in area 2) divides into two, creating a northwest branching. In Figure 14 the branching is visible in the ISW satellite measurements. The mode-2 baroclinic fluxes coming from D and A have a more dissociate path (Tchilibou et al., 2022) compared to mode-1. In Figure 7, the identification of mode-2 ISW signatures coming from D is more evident than for mode-1.

A synthesis of the mode-1 and mode-2 ISW propagation direction and velocity according to the different seasons can be found in Figure 16.
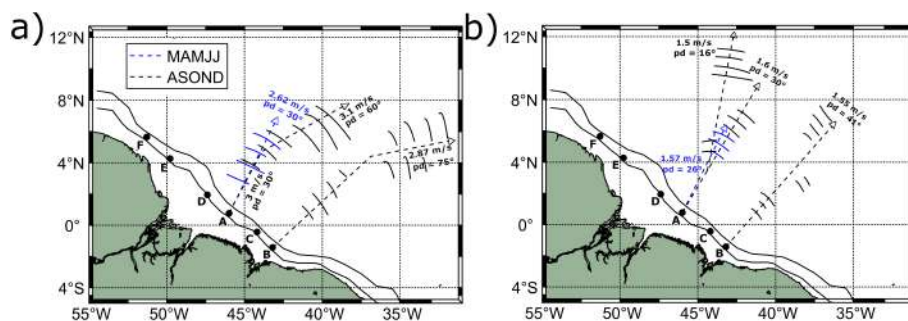
Figure 16. Synthesis of the (a) mode-1 and mode-2 (b) ISW propagation direction and velocity according to the different seasons.

Aliasing effect

It is important to point out that we cannot rule out the sampling restrictions due to the aliasing effect connected to the sun-synchronous satellite orbit which can result in images acquired during a similar flood–ebb phase of the semi-diurnal tide (da Silva et al., 2015) and to the location of the sun glint areas. Further analysis can be performed focusing on the construction in the study area of a more balanced data set according to both the different seasons and wave baroclinic modes by considering the use of different optical sensors/satellites such as MODIS/AQUA, MSI/Sentinel-2, and OLCI/Sentinel-3.

Author contributions. The remote sensing data processing was made by C.R.d.M., C.A.D.L., and M.C.B.R. with help of T.K.T. Tide simulation was made by A.K.L. Analysis was performed and discussed by C.R.d.M. with help of A.K.L., V.V., J.C.B.d.S., J.M.M., and C.A.D.L. The manuscript was written with help of all authors.

Competing interests. The authors declare that they have no known competing financial interests or personal relationships that could have appeared to influence the work reported in this paper.

390 *Financial support.* This work and the CDD contract from C.R.d.M. were supported by CNES funding in the frame of the APR TOSCA MIAMAZ TOSCA project, PI A.K.L., V.V., and Isabelle Dadou. C.A.D.L. is funded by the Ministry of Science, Technology, and Innovation and the Brazilian Navy (CNPQ/MCTI 06/2020 - grant), and the research project AtlantECO (H2020 BG-08-2018-2019, grant agreement N°862923). M.C.B.R. is funded by the Coordenação de Aperfeiçoamento de Pessoal de Nível Superior – Brasil (CAPES) – Finance Code 001. J.C.B.d.S. is funded by the Portuguese funding agency Fundação para a Ciência e Tecnologia (FCT) under project IDB/04683/2020.

395 J.M.M. is supported by FCT – Portuguese Foundation for Science and Technology under contracts UIDB/04423/2020 and UIDP/04423/2020.

Acknowledgements. The authors would like to thank NASA's Earth Science Data System, ESDS for providing the MODIS/TERRA data, and the Mercator Ocean International as part of the Copernicus Programme for providing the Global Ocean Ensemble Physics Reanalysis (EPR) data. The authors would like to thank Dr. Luc Rainville from the University of Washington, Seattle, WA, USA for sharing your knowledge in the topic with us. This work contributes to the project "Amazomix" under the DOI: 10.17600/18001364

400 https://campagnes.flotteoceanographique.fr/campagnes/18001364/.

Appendix A: Viscous Taylor-Goldstein Equation

Considering a horizontal wave vector $\mathbf{k}$ on a horizontal background flow $\mathbf{U}_h = \{u(z), v(z)\}$, for a small-amplitude and normal mode disturbance, the component of the background flow parallel to the wave vector rules the mode evolution (Lian et al., 2020):

$$U = \frac{\mathbf{k} \cdot \mathbf{U}_h}{k} \tag{A1}$$

where $k = \sqrt{k_z^2 + k_m^2}$ is the wave number magnitude, with k_z and k_m being a real wave number with zonal and meridional components. The buoyancy is defined as $b = g(\rho_0 - \rho)/\rho_0$, where g is the gravitational acceleration and ρ_0 is the characteristic value of the density ρ. The vertical velocity perturbation and the buoyancy perturbation (i. e., w' and b', respectively) are considered to disturb the parallel shear flow $U(z)$ (Lian et al., 2020).

$$b' = \Re\left(\hat{b}(z) e^{\sigma t + ikx}\right) \tag{A2}$$

$$w' = \Re\left(\hat{w}(z) e^{\sigma t + ikx}\right) \tag{A3}$$

The terms $\Re$ and $\Im$ refer to the real and imaginary parts, respectively, and $i = \sqrt{-1}$. The complex vertical structure functions of vertical buoyancy and velocity are, respectively, $\hat{b}$ and $\hat{w}$. σ is the complex growth rate and x is the horizontal coordinate parallel to the wave vector. The effects of viscosity and diffusivity (respectively, A_h, A_v and K_h, K_v where the subscripts

415   h and v mean horizontal and vertical components, respectively) are included and their linearized normal-mode equations are (Liu, 2010; Lian et al., 2020):

$$(\sigma + ikU)\nabla^2 \hat{w} - ik\frac{d^2U}{dz^2}\hat{w} = T_w\hat{w} - k^2\hat{b}, \tag{A4}$$

$$(\sigma + ikU)\hat{b} + \frac{dB}{dz}\hat{w} = T_b\hat{b} \tag{A5}$$

with viscous and diffusive operators

420   $$T_w = \frac{d^2}{dz^2}\left(A_v\frac{d^2}{dz^2}\right) - k^2\frac{d}{dz}\left[(A_h + A_v)\frac{d}{dz}\right] + k^4A_h, \tag{A6}$$

$$T_b = \frac{d}{dz}\left(K_v\frac{d}{dz}\right) - k^2K_h \tag{A7}$$

Thus, we can deal with the viscous TGE (Equations A4 - A7) as a generalized differential eigenvalue problem:

$$\sigma\begin{pmatrix}\nabla^2 & \mathbf{0} \\ \mathbf{0} & \mathbf{I}\end{pmatrix}\begin{pmatrix}\hat{w} \\ \hat{b}\end{pmatrix} = \begin{pmatrix}-ikU\nabla^2 + ik\frac{d^2U}{dz^2} + T_w & -k^2 \\ -\frac{dB}{dz} & -ikU + T_b\end{pmatrix}\begin{pmatrix}\hat{w} \\ \hat{b}\end{pmatrix} \tag{A8}$$

where $\mathbf{0}$ and $\mathbf{I}$ are the zero and identity matrices, respectively. Considering, $\nabla^2 = d^2/dz^2 - k^2$, the boundary conditions as

425   $\hat{w} = 0$ (impermeable) and $\hat{b} = 0$ (constant buoyancy).

The phase speed of internal gravity waves is described as (Smyth et al., 2011; Lian et al., 2020):

$$c = \frac{w}{k} \tag{A9}$$

where $w = -\Im(\sigma)$, and σ is the eigenvalue of Equation A8. The Coriolis force due to the Earth's rotation is not taken into account by Lian's method. However, in our study area, this effect can be neglected due to the proximity to the Equator. Lian's

430 method includes the effects of viscosity and diffusivity, which in origin we choose to be the kinematic viscosity and the thermal diffusivity of water at 20°C (respectively, 1 cSt or 10^{-6} m.s^{-1}, and $1.43\text{x}10^{-7}$ m.s^{-1}). We have done tests using viscosity equal to zero and for internal tidal waves (of various modes) it does not make any difference, suggesting that in this case inviscid TGE could as well be used.

The underestimation of the ISW phase velocity calculated using the TGE is expected since the equation calculates linear

435 wave phase speed and the nonlinear effects increase the speed of the linear waves (Alford et al., 2010; da Silva et al., 2011). The nonlinear phase speed can be corrected using the Korteweg–De Vries (KdV) equation (Hammack and Segur, 1974; Alford et al., 2010), however, this theory applies only to shallow waters with uniform depths which is not the case in our study area. The KdV equation would increase the mean wave speed by about 16% for mode-1 waves, considering a maximum wave elevation of 100 m (wave elevation taking from Brandt et al. (2002)).

References

Aguedjou, H., Dadou, I., Chaigneau, A., Morel, Y., and Alory, G.: Eddies in the Tropical Atlantic Ocean and their seasonal variability, Geophysical Research Letters, 46, 12 156–12 164, 2019.

Alford, M. H., Lien, R.-C., Simmons, H., Klymak, J., Ramp, S., Yang, Y. J., Tang, D., and Chang, M.-H.: Speed and evolution of nonlinear internal waves transiting the South China Sea, Journal of Physical Oceanography, 40, 1338–1355, 2010.

Alford, M. H., Peacock, T., MacKinnon, J. A., Nash, J. D., Buijsman, M. C., Centurioni, L. R., Chao, S.-Y., Chang, M.-H., Farmer, D. M., Fringer, O. B., et al.: The formation and fate of internal waves in the South China Sea, Nature, 521, 65–69, 2015.

Alpers, W.: Theory of radar imaging of internal waves, Nature, 314, 245–247, 1985.

Bai, X., Lamb, K. G., and da Silva, J. C.: Small-Scale Topographic Effects on the Generation of Along-Shelf Propagating Internal Solitary Waves on the Amazon Shelf, Journal of Geophysical Research: Oceans, 126, e2021JC017 252, 2021.

Barbot, S., Lyard, F., Tchilibou, M., and Carrere, L.: Background stratification impacts on internal tide generation and abyssal propagation in the western equatorial Atlantic and the Bay of Biscay, Ocean Science, 17, 1563–1583, 2021.

Brandt, P., Rubino, A., and Fischer, J.: Large-amplitude internal solitary waves in the North Equatorial Countercurrent, Journal of Physical Oceanography, 32, 1567–1573, 2002.

da Silva, J., New, A., and Magalhães, J.: On the structure and propagation of internal solitary waves generated at the Mascarene Plateau in the Indian Ocean, Deep Sea Research Part I: Oceanographic Research Papers, 58, 229–240, 2011.

da Silva, J., Buijsman, M., and Magalhães, J.: Internal waves on the upstream side of a large sill of the Mascarene Ridge: A comprehensive view of their generation mechanisms and evolution, Deep Sea Research Part I: Oceanographic Research Papers, 99, 87–104, 2015.

da Silva, J. C., Magalhães, J., Buijsman, M. C., and Garcia, C.: SAR imaging of wave tails: Recognition of second mode internal wave patterns and some mechanisms of their formation, Living Plannet Symposium 2016, 2016.

Dunphy, M., Ponte, A. L., Klein, P., and Le Gentil, S.: Low-mode internal tide propagation in a turbulent eddy field, Journal of Physical Oceanography, 47, 649–665, 2017.

Farmer, D. M. and Smith, J. D.: Tidal interaction of stratified flow with a sill in Knight Inlet, Deep Sea Research Part A. Oceanographic Research Papers, 27, 239–254, 1980.

Gerkema, T.: Internal and interfacial tides: beam scattering and local generation of solitary waves, Journal of Marine Research, 59, 227–255, 2001.

Guo, C., Vlasenko, V., Alpers, W., Stashchuk, N., and Chen, X.: Evidence of short internal waves trailing strong internal solitary waves in the northern South China Sea from synthetic aperture radar observations, Remote Sensing of Environment, 124, 542–550, 2012.

Hammack, J. L. and Segur, H.: The Korteweg-de Vries equation and water waves. Part 2. Comparison with experiments, Journal of Fluid mechanics, 65, 289–314, 1974.

Helfrich, K. R. and Melville, W.: On long nonlinear internal waves over slope-shelf topography, Journal of Fluid Mechanics, 167, 285–308, 1986.

Huthnance, J. M.: Circulation, exchange and water masses at the ocean margin: the role of physical processes at the shelf edge, Progress in Oceanography, 35, 353–431, 1995.

Hyder, P., Jeans, D., Cauquil, E., and Nerzic, R.: Observations and predictability of internal solitons in the northern Andaman Sea, Applied Ocean Research, 27, 1–11, 2005.

Jackson, C. R. and Alpers, W.: The role of the critical angle in brightness reversals on sunglint images of the sea surface, Journal of Geophysical Research: Oceans, 115, 2010.

Jackson, C. R., da Silva, J. C., and Jeans, G.: The generation of nonlinear internal waves, Oceanography, 25, 108–123, 2012.

Jeans, D.: Solitary internal waves in the ocean: A literature review completed as part of the internal wave contribution to Morena. UCES, Marine Science Labs, University of North Wales. Rep. U-95, 1995.

Kudryavtsev, V., Myasoedov, A., Chapron, B., Johannessen, J. A., and Collard, F.: Joint sun-glitter and radar imagery of surface slicks, Remote sensing of environment, 120, 123–132, 2012.

Lamb, K. and Warn-Varnas, A.: Two-dimensional numerical simulations of shoaling internal solitary waves at the ASIAEX site in the South China Sea, Nonlinear Processes in Geophysics, 22, 289–312, 2015.

Lentini, C. A., Magalhães, J. M., da Silva, J. C., and Lorenzzetti, J. A.: Transcritical flow and generation of internal solitary waves off the Amazon River: Synthetic aperture radar observations and interpretation, Oceanography, 29, 187–195, 2016.

Lian, Q., Smyth, W. D., and Liu, Z.: Numerical computation of instabilities and internal waves from in situ measurements via the viscous Taylor–Goldstein problem, Journal of Atmospheric and Oceanic Technology, 37, 759–776, 2020.

Liang, J. and Li, X.-M.: Generation of second-mode internal solitary waves during winter in the northern South China Sea, Ocean Dynamics, 69, 313–321, 2019.

Liang, J., Du, T., Li, X., and He, M.: Generation of mode-2 internal waves in a two-dimensional stratification by a mode-1 internal wave, Wave Motion, 83, 227–240, 2018.

Liu, A. K., Su, F.-C., Hsu, M.-K., Kuo, N.-J., and Ho, C.-R.: Generation and evolution of mode-two internal waves in the South China Sea, Continental Shelf Research, 59, 18–27, 2013.

Liu, B. and D'Sa, E. J.: Oceanic internal waves in the Sulu–Celebes Sea under sunglint and moonglint, IEEE Transactions on Geoscience and Remote Sensing, 57, 6119–6129, 2019.

Liu, B., Yang, H., Ding, X., and Li, X.: Tracking the internal waves in the South China Sea with environmental satellite sun glint images, Remote sensing letters, 5, 609–618, 2014.

Liu, Z.: Instability of baroclinic tidal flow in a stratified fjord, Journal of physical oceanography, 40, 139–154, 2010.

Magalhaes, J., Da Silva, J., and Buijsman, M. C.: Long lived second mode internal solitary waves in the Andaman Sea, Scientific Reports, 10, 10 234, 2020.

Magalhães, J. M. and da Silva, J. C.: Internal solitary waves in the Andaman Sea: New insights from SAR imagery, Remote Sensing, 10, 861, 2018.

Magalhães, J. M., da Silva, J., Buijsman, M. C., and Garcia, C.: Effect of the North Equatorial Counter Current on the generation and propagation of internal solitary waves off the Amazon shelf (SAR observations), Ocean Science, 12, 243–255, 2016.

Moum, J. N., Nash, J. D., and Klymak, J. M.: Small-scale processes in the coastal ocean, Oceanography, 21, 22–33, 2008.

Muacho, S., da Silva, J., Brotas, V., and Oliveira, P.: Effect of internal waves on near-surface chlorophyll concentration and primary production in the Nazaré Canyon (west of the Iberian Peninsula), Deep Sea Research Part I: Oceanographic Research Papers, 81, 89–96, 2013.

Munk, W. and Wunsch, C.: Abyssal recipes II: Energetics of tidal and wind mixing, Deep Sea Research Part I: Oceanographic Research Papers, 45, 1977–2010, 1998.

New, A. and da Silva, J.: Remote-sensing evidence for the local generation of internal soliton packets in the central Bay of Biscay, Deep Sea Research Part I: Oceanographic Research Papers, 49, 915–934, 2002.

Osborne, A., Burch, T., and Scarlet, R.: The influence of internal waves on deep-water drilling, Journal of Petroleum Technology, 30, 1497–1504, 1978.

Rainville, L. and Pinkel, R.: Propagation of low-mode internal waves through the ocean, Journal of Physical Oceanography, 36, 1220–1236, 2006.

Richardson, P., Hufford, G., Limeburner, R., and Brown, W.: North Brazil current retroflection eddies, Journal of Geophysical Research: Oceans, 99, 5081–5093, 1994.

Richardson, P. L. and Walsh, D.: Mapping climatological seasonal variations of surface currents in the tropical Atlantic using ship drifts, Journal of Geophysical Research: Oceans, 91, 10 537–10 550, 1986.

Rosa, M. C. B., Moura, P. V., de Mendonça, L. F. F., and Lentini, C. A. D.: Mapeamento e caracterização de ondas internas ao largo da foz do rio Amazonas através do sensor modis-satélite terra (2008 a 2019), Brazilian Journal of Development, 7, 21 164–21 179, 2021.

Sandstrom, H. and Elliott, J.: Internal tide and solitons on the Scotian Shelf: A nutrient pump at work, Journal of Geophysical Research: Oceans, 89, 6415–6426, 1984.

Silva, A., Araujo, M., Medeiros, C., Silva, M., and Bourles, B.: Seasonal changes in the mixed and barrier layers in the western equatorial Atlantic, Brazilian Journal of Oceanography, 53, 83–98, 2005.

Smyth, W., Moum, J., and Nash, J.: Narrowband oscillations in the upper equatorial ocean. Part II: Properties of shear instabilities, Journal of Physical Oceanography, 41, 412–428, 2011.

Tchilibou, M., Koch-Larrouy, A., Barbot, S., Lyard, F., Morel, Y., Jouanno, J., and Morrow, R.: Internal tides off the Amazon shelf during two contrasted seasons: Interactions with background circulation and SSH imprints, Ocean Science Discussions, pp. 1–38, 2022.

Vlasenko, V., Guo, C., and Stashchuk, N.: On the mechanism of A-type and B-type internal solitary wave generation in the northern South China Sea, Deep Sea Research Part I: Oceanographic Research Papers, 69, 100–112, 2012.

Yang, Y. J., Fang, Y. C., Chang, M.-H., Ramp, S. R., Kao, C.-C., and Tang, T. Y.: Observations of second baroclinic mode internal solitary waves on the continental slope of the northern South China Sea, Journal of Geophysical Research: Oceans, 114, 2009.

Zhang, X. and Li, X.: Satellite data-driven and knowledge-informed machine learning model for estimating global internal solitary wave speed, Remote Sensing of Environment, 283, 113 328, 2022.